

Chapter 2

Building a Nonlinear Rotary-Wing Aircraft Model

2.1 Introduction

This chapter focuses on nonlinear flight dynamic modeling of rotary-wing aircraft. The intention is to establish a general modeling framework, that applies to not only traditional single main-rotor helicopters, but also unconventional rotary-wing aircraft. Apart from general equations of motion, the modeling framework relies heavily on and is extended from the results in [97]. Differing from a traditional modeling description, the inflow dynamics of a rotor module include latest result from [13] to handle a rotor in descent motion. In addition, a propeller thrust and torque calculation procedure is illustrated using the typical nomenclature in helicopter theory books. For the purposes of easy implementation and simple writing format, vector description of equations is utilized whenever possible.

2.2 General Equations of Motion

Assumptions associated with the classical six degree-of-freedom (DOF) equations of motion include rigid body dynamics and insignificant effects from Earth's curvature and rotation. These two assumptions are usually satisfied for applications in performance study, stability analysis, dynamic simulation, control system design, and handling qualities assessment.

Typically, the general equations of motion include four sets of equations: force equation, moment equation, kinematic equation, and navigation equation.

2.2.1 Force Equation

Figure 2.1 shows typical coordinate systems for both aircraft body and the main rotor hub. Let u_B , v_B , and w_B be three velocity components and p_B , q_B , and r_B

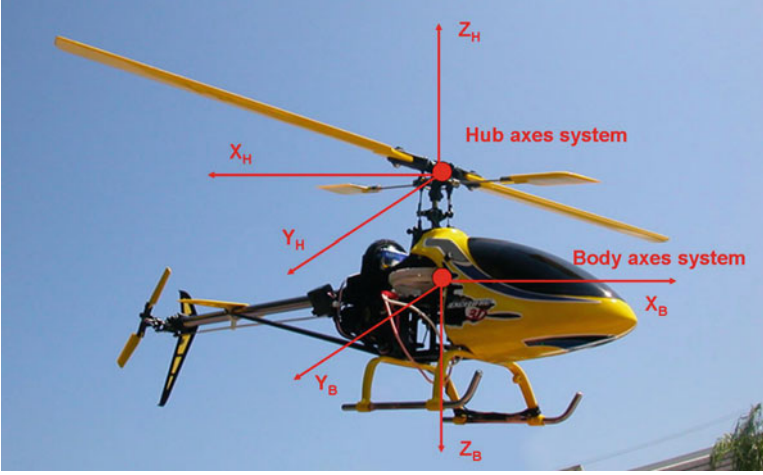


Fig. 2.1 Definitions of body axes and hub axes system (Image with courtesy of <http://cheaprchicopters.net>)

be three angular rate components along the x -, y -, z -axis in the body axes system, respectively. Furthermore, define the Euler angle representation as roll (ϕ), pitch (θ), and yaw (ψ). The force equation is listed as follows:

$$\begin{bmatrix} \dot{u}_B \\ \dot{v}_B \\ \dot{w}_B \end{bmatrix} = - \begin{bmatrix} p_B \\ q_B \\ r_B \end{bmatrix} \times \begin{bmatrix} u_B \\ v_B \\ w_B \end{bmatrix} + \left(\begin{bmatrix} -g \sin \theta \\ g \sin \phi \cos \theta \\ g \cos \phi \cos \theta \end{bmatrix} + \frac{1}{m} \begin{bmatrix} F_x \\ F_y \\ F_z \end{bmatrix} \right) \quad (2.1)$$

The cross-product term is the Coriolis acceleration due to body rotation. There are two contributions to the force term of the equation: one is the gravitational force resolved in the body axes system, and another is all other forces in the body axes system, represented as F_x , F_y , and F_z .

2.2.2 Moment Equation

Define L , M , and N as the resultant rolling, pitching, and yawing moments along the x -, y -, z -axis in the body axes system, respectively. The moment equation is:

$$\begin{bmatrix} \dot{p}_B \\ \dot{q}_B \\ \dot{r}_B \end{bmatrix} = -I^{-1} \left(\begin{bmatrix} p_B \\ q_B \\ r_B \end{bmatrix} \times \left(I \begin{bmatrix} p_B \\ q_B \\ r_B \end{bmatrix} \right) \right) + I^{-1} \begin{bmatrix} L \\ M \\ N \end{bmatrix} \quad (2.2)$$

The inertial matrix, I , can be represented as

$$I = \begin{bmatrix} I_{xx} & 0 & -I_{xz} \\ 0 & I_{yy} & 0 \\ -I_{xz} & 0 & I_{zz} \end{bmatrix}, \quad I^{-1} = \frac{1}{\Gamma} \begin{bmatrix} I_{zz} & 0 & I_{xz} \\ 0 & \Gamma & 0 \\ I_{xz} & 0 & I_{xx} \end{bmatrix} \quad (2.3)$$

where $\Gamma = I_{xx}I_{zz} - I_{xz}^2$. In the moment equation, the first term on the right-hand side includes both inertial coupling and gyroscopic effect. Notice that in the I matrix, there are no coupling terms I_{yz} and I_{xy} . This is due to the fact that for most flying vehicles, the $x - z$ plane is a plane of symmetry. Although, strictly speaking, a classical single main-rotor helicopter has no plane of symmetry due to its tail rotor, it is often used to simplify the resultant equations. The inertial coupling term associated with I_{xz} will be significant in the case of highly maneuverable motions. In some special cases with three symmetric planes like quad-rotor system, there is no inertial coupling presented in their motions. While gyroscopic effect is evident for a single-engine fixed-wing aircraft in maneuvering flight, it is even more significant in a rotary-wing vehicle due to its main rotor. In fact, the moment due to gyroscopic effect is the main source of roll and pitch dampings from the rotor in an unaugmented rotorcraft.

2.2.3 Kinematic Equation

It should be pointed out that the three Euler angle derivatives, $\dot{\phi}$, $\dot{\theta}$, and $\dot{\psi}$, are not orthogonal to each other. The relationship between Euler angle derivatives and body angular rates is provided as follows:

$$\begin{bmatrix} \dot{\phi} \\ \dot{\theta} \\ \dot{\psi} \end{bmatrix} = \begin{bmatrix} 1 & \tan \theta \sin \phi & \tan \theta \cos \phi \\ 0 & \cos \phi & -\sin \phi \\ 0 & \frac{\sin \phi}{\cos \theta} & \frac{\cos \phi}{\cos \theta} \end{bmatrix} \begin{bmatrix} p_B \\ q_B \\ r_B \end{bmatrix} \quad (2.4)$$

It is noted that the kinematic equation has a singularity at $\theta = 90^\circ$. For all-attitude flight, a quaternion representation is recommended.

2.2.4 Navigation Equation

The navigation equation is represented in the local NED (North–East–Down) frame. The transformation from the vehicle's body frame to the local NED frame follows

the predefined rotational sequence: roll, pitch, and yaw. Therefore, the navigation equation is

$$\begin{bmatrix} \dot{x}_N \\ \dot{x}_E \\ \dot{x}_D \end{bmatrix} = \begin{bmatrix} \cos \psi & -\sin \psi & 0 \\ \sin \psi & \cos \psi & 0 \\ 0 & 0 & 1 \end{bmatrix} \begin{bmatrix} \cos \theta & 0 & \sin \theta \\ 0 & 1 & 0 \\ -\sin \theta & 0 & \cos \theta \end{bmatrix} \begin{bmatrix} 1 & 0 & 0 \\ 0 & \cos \phi & -\sin \phi \\ 0 & \sin \phi & \cos \phi \end{bmatrix} \begin{bmatrix} u_B \\ v_B \\ w_B \end{bmatrix} \quad (2.5)$$

In practical applications, position information is often obtained in terms of GPS data in the Geodetic form (longitude, latitude, and height). In such cases, transformations can be carried out first from Geodetic frame to ECEF (Earth centered Earth fixed) frame, and then to local NED frame.

In both force and moment equations, the resultant forces (F_x , F_y , and F_z) and moments (L , M , and N) are contributions from various modules of a rotary-wing aircraft, including main rotor, tail rotor (for a classical helicopter), propeller (if mounted, typically with a compound helicopter or an autogyro), fuselage, horizontal and vertical tails, wing (if mounted), landing gear, and slung loads (for underslung operation). In the case of aerodynamic forces and moments, they are typically computed in the local wind axes system. This process requires that the relevant motion variables be transformed to the wind axes system and resultant forces and moments be transformed back to the body axes system.

A block diagram for a general rotorcraft model is provided in Fig. 2.2, showcasing the relationship between each individual module and general equations of motion. Typically, the general equations of motion take forces and moments transformed from each module and update the motion variables at each time step. The motion variables are fed back into each module through appropriate transformations to generate the updated forces and moments.

In the next section, the main characteristics of each module in Fig. 2.2 will be analyzed. It shall be emphasized that although the study uses a helicopter as a baseline platform, it can be extended to unconventional rotorcraft platforms. Readers are encouraged to explore the use of modeling and simulation to evaluate advanced or novel rotorcraft concepts and applications.

2.3 Modular-Based Modeling

2.3.1 Main Rotor

General assumptions associated with flight dynamic modeling for the main rotor are [97]

- Small angle approximation. This is applied to the blade flapping angle and inflow angle used during the derivation.

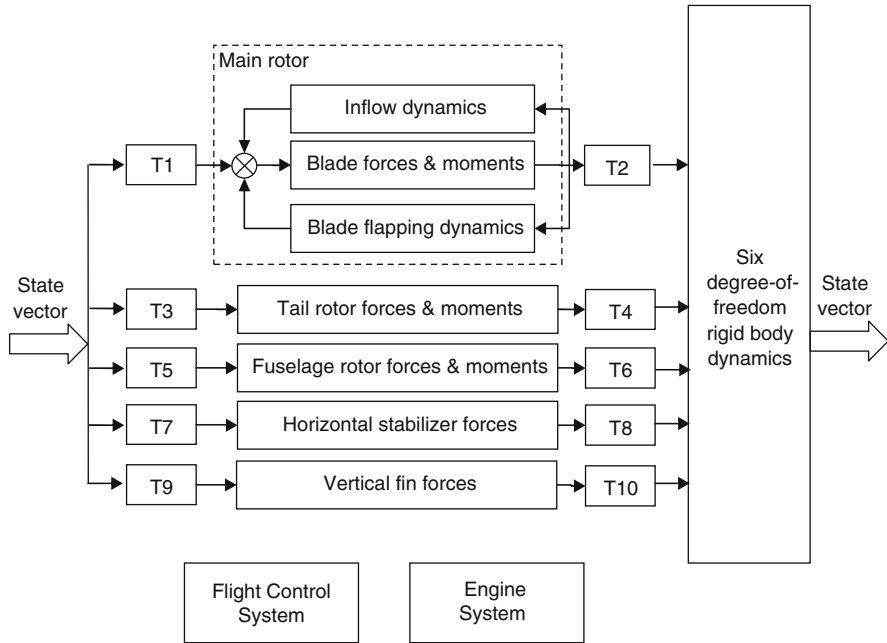


Fig. 2.2 Block diagram for a general rotorcraft model [97]

- **Rigid blade.** This assumption is valid for flight dynamic applications including performance estimation, trim study, stability and control analysis, handling quality assessment, and dynamic response simulation. Elastic blade modeling or even finite element blade modeling are only justified when flexibility of the blade is essential.
- **Reverse flow region, stall, and compressibility effects are ignored.** These effects are only appreciable during high forward speed. A criteria for judging the boundary speed is that the maximum tip speed for the advancing blade should not exceed 60 – 70% of the speed of sound.
- **First harmonic approximation to the blade flapping.** In this case, the blade flapping angle is determined by coning angle β_0 , longitudinal first harmonic term β_{1c} (positive backward), and lateral first harmonic term β_{1s} (positive toward the advancing side). Mathematically, the blade flapping angle is represented by

$$\beta = \beta_0 - \beta_{1c} \cos \psi - \beta_{1s} \sin \psi \quad (2.6)$$

where ψ is the blade azimuthal angle.

- **Quasi-steady flapping dynamics.** The rotor would respond to continuously changing motions as if they were a sequence of steady conditions. Mathematically, it assumes that the terms $\frac{dp}{d\psi}$ and $\frac{dq}{d\psi}$ are insignificant in determining the rotor first-harmonic terms.

- Uniform inflow and no inflow dynamics.
- No tip losses.

With the above assumptions, the rotor model introduced in this section is valid for an advance ratio μ , computed using rotor forward speed divided by blade tip speed at hover, up to 0.3.

2.3.2 Transformation from Body to Hub

As a first step, motion variables including translational velocities and angular rates are transformed into the hub axis system (as shown in Fig. 2.1). The velocity transformations involve a rotation with respect to the body y-axis due to the forward tilting of rotor shaft i_s , and the contribution from angular rates to the translational velocities due to spatial separation between the body center of gravity (C.G.) and the main rotor hub.

$$\begin{bmatrix} u_H \\ v_H \\ w_H \end{bmatrix} = \begin{bmatrix} \cos i_s & 0 & \sin i_s \\ 0 & 1 & 0 \\ -\sin i_s & 0 & \cos i_s \end{bmatrix} \left(\begin{bmatrix} u_B \\ v_B \\ w_B \end{bmatrix} + \begin{bmatrix} STA_H - STA_{CG} \\ BL_H - BL_{CG} \\ WL_H - WL_{CG} \end{bmatrix} \times \begin{bmatrix} p_B \\ q_B \\ r_B \end{bmatrix} \right) \quad (2.7)$$

where STA, BL, and WL are the stationline, buttline, and waterline for a sub-system (*e.g.*, the main rotor hub), respectively. The subscript H stands for the main rotor hub. Similarly, the angular rate transformation involves the rotation with respect to body y-axis due to forward tilting of the rotor shaft,

$$\begin{bmatrix} p_H \\ q_H \\ r_H \end{bmatrix} = \begin{bmatrix} \cos i_s & 0 & \sin i_s \\ 0 & 1 & 0 \\ -\sin i_s & 0 & \cos i_s \end{bmatrix} \begin{bmatrix} p_B \\ q_B \\ r_B \end{bmatrix} \quad (2.8)$$

2.3.3 Blade Flapping Dynamics

The blade flapping dynamics are described by a second-order differential equation [97]

$$\begin{bmatrix} \ddot{\beta}_0 \\ \ddot{\beta}_{1c} \\ \ddot{\beta}_{1s} \end{bmatrix} + D \begin{bmatrix} \dot{\beta}_0 \\ \dot{\beta}_{1c} \\ \dot{\beta}_{1s} \end{bmatrix} + K \begin{bmatrix} \beta_0 \\ \beta_{1c} \\ \beta_{1s} \end{bmatrix} = F \quad (2.9)$$

where

$$D = \Omega \begin{bmatrix} \frac{\gamma}{2}(\frac{1}{4} - \frac{2}{3}\epsilon + \frac{\epsilon^2}{2}) & 0 & -\frac{\gamma\mu}{4}(\frac{1}{3} - \epsilon + \epsilon^2) \\ 0 & \frac{\gamma}{2}(\frac{1}{4} - \frac{2}{3}\epsilon + \frac{\epsilon^2}{2}) & 2 \\ -\frac{\gamma\mu}{2}(\frac{1}{3} - \epsilon + \epsilon^2) & -2 & \frac{\gamma}{2}(\frac{1}{4} - \frac{2}{3}\epsilon + \frac{\epsilon^2}{2}) \end{bmatrix} \quad (2.10)$$

$$K = \Omega^2 \begin{bmatrix} P^2 + \frac{\gamma K_1 \mu^2}{4}(\frac{1}{2} - \epsilon + \frac{\epsilon^2}{2}) & -\frac{\gamma\mu}{4}(\frac{\epsilon}{2} - \epsilon^2) & -\frac{\gamma K_1 \mu}{4}(\frac{2}{3} - \epsilon) \\ -\frac{\gamma\mu}{2}(\frac{1}{3} - \frac{\epsilon}{2}) & P^2 - 1 + \frac{\gamma K_1 \mu^2}{8}(\frac{1}{2} - \epsilon + \frac{\epsilon^2}{2}) & \frac{\gamma}{2}(\frac{1}{4} - \frac{2}{3}\epsilon + \frac{\epsilon^2}{2}) + \frac{\gamma\mu^2}{8}(\frac{1}{2} - \epsilon + \frac{\epsilon^2}{2}) \\ -\frac{\gamma K_1 \mu}{2}(\frac{2}{3} - \epsilon) & -\frac{\gamma}{2}(\frac{1}{4} - \frac{2}{3}\epsilon + \frac{\epsilon^2}{2}) + \frac{\gamma\mu^2}{8}(\frac{1}{2} - \epsilon + \frac{\epsilon^2}{2}) & P^2 - 1 + \frac{3}{8}\gamma K_1 \mu^2(\frac{1}{2} - \epsilon + \frac{\epsilon^2}{2}) \end{bmatrix} \quad (2.11)$$

$$F = \Omega^2 \left\{ \begin{bmatrix} -\frac{M_\beta}{I_\beta \Omega^2} \\ 0 \\ 0 \end{bmatrix} + \begin{bmatrix} \frac{\gamma}{2}[(\frac{1}{5} - \frac{\epsilon}{4}) + \frac{\mu^2}{2}(\frac{1}{3} - \frac{\epsilon}{2})] \\ 0 \\ -\frac{\gamma\mu}{2}(\frac{1}{2} - \frac{2}{3}\epsilon) \end{bmatrix} \theta_t + \begin{bmatrix} \frac{\gamma}{2}(\frac{1}{3} - \frac{\epsilon}{2}) \\ 0 \\ -\frac{\gamma\mu}{2}(\frac{1}{2} - \epsilon + \frac{\epsilon^2}{2}) \end{bmatrix} \lambda \right. \\ + \begin{bmatrix} \frac{\gamma}{2}[(\frac{1}{4} - \frac{\epsilon}{3}) + \frac{\mu^2}{2}(\frac{1}{2} - \epsilon + \frac{\epsilon^2}{2})] & 0 & -\frac{\gamma}{2}[\mu(\frac{1}{3} - \frac{\epsilon}{2})] \\ 0 & \frac{\gamma}{2}[(\frac{1}{4} - \frac{\epsilon}{3}) + \frac{\mu^2}{4}(\frac{1}{2} - \epsilon + \frac{\epsilon^2}{2})] & 0 \\ -\frac{\gamma}{2}\mu(\frac{2}{3} - \epsilon) & 0 & \frac{\gamma}{2}[(\frac{1}{4} - \frac{\epsilon}{3}) + \frac{3\mu^2}{4}(\frac{1}{2} - \epsilon + \frac{\epsilon^2}{2})] \end{bmatrix} \begin{bmatrix} \theta_0 \\ \theta_{1c} \\ \theta_{1s} \end{bmatrix} \\ \left. + \begin{bmatrix} \frac{\gamma}{8}\mu(\frac{2}{3} - \epsilon) & 0 \\ -2(1 + \frac{eM_\beta}{gI_\beta}) & \frac{\gamma}{2}(\frac{1}{4} - \frac{\epsilon}{3}) \\ -\frac{\gamma}{2}(\frac{1}{4} - \frac{\epsilon}{3}) & -2(1 + \frac{eM_\beta}{gI_\beta}) \end{bmatrix} \begin{bmatrix} \frac{p_H}{\Omega} \cos \beta_w + \frac{q_H}{\Omega} \sin \beta_w \\ \frac{p_H}{\Omega} \sin \beta_w - \frac{q_H}{\Omega} \cos \beta_w \end{bmatrix} \right\} \quad (2.12)$$

with the parameters defined as

- θ_0 = collective pitch angle
- θ_{1s} = longitudinal cyclic pitch angle
- θ_{1c} = lateral cyclic pitch angle
- Ω = rotor rotational speed
- γ = blade lock number
- θ_t = blade twist
- λ = total inflow ratio
- β_w = rotor sideslip angle, $\text{asin}(\frac{v_H}{\sqrt{u_H^2 + v_H^2}})$, defined as 0 if $u_H = v_H = 0$.

In (2.11), P represents the ratio of flapping frequency to rotor speed

$$P^2 = 1 + \frac{eM_\beta}{gI_\beta} + \frac{K_\beta}{I_\beta\Omega^2} + \frac{\gamma K_1}{8} \left(1 - \frac{4}{3}\epsilon\right) \quad (2.13)$$

where e , K_β , and K_1 represent flapping hinge offset, flap spring, and pitch-flap coupling, respectively. $\epsilon = \frac{e}{R}$ is the non-dimensionalized hinge offset ratio. The term M_β in the above equation represents blade weight moment. For a blade with uniform mass distribution, the simple relationship between M_β and blade moment of inertia I_β can be established [44]:

$$M_\beta = \frac{3g}{2R} I_\beta \quad (2.14)$$

Without hinge offset, flap spring, and pitch-flap coupling, the flap frequency is the same as the rotor frequency. With either hinge offset (typically with articulated rotor, or hingeless rotor), or flap spring (normally coupled with a teetering rotor), or the pitch-flap coupling (normally with a tail rotor), the flap frequency is raised above the rotor frequency, with typical value $P = 1.0 - 1.2$ [44].

While (2.9) is derived based on a general rotor configuration, simplifications can be made on a number of cases, which in turn provides important physical insights on the rotor flapping motion. In the first simplification, it is assumed that the rotor has zero hinge offset, no flap spring, and no pitch-flap coupling. Equation (2.9) can thus be re-written:

$$\begin{bmatrix} \ddot{\beta}_0 \\ \ddot{\beta}_{1c} \\ \ddot{\beta}_{1s} \end{bmatrix} + \Omega \begin{bmatrix} \frac{\gamma}{8} & 0 & -\frac{\gamma\mu}{12} \\ 0 & \frac{\gamma}{8} & 2 \\ -\frac{\gamma\mu}{6} & -2 & \frac{\gamma}{8} \end{bmatrix} \begin{bmatrix} \dot{\beta}_0 \\ \dot{\beta}_{1c} \\ \dot{\beta}_{1s} \end{bmatrix} + \Omega^2 \begin{bmatrix} 1 & 0 & 0 \\ -\frac{\gamma\mu}{6} & 0 & \frac{\gamma}{8} + \frac{\gamma\mu^2}{16} \\ 0 & -\frac{\gamma}{8} + \frac{\gamma\mu^2}{16} & 0 \end{bmatrix} \begin{bmatrix} \beta_0 \\ \beta_{1c} \\ \beta_{1s} \end{bmatrix}$$

$$= \Omega^2 \begin{bmatrix} -\frac{M_\beta}{I_\beta \Omega^2} + \frac{\gamma}{8}(1 + \mu^2)\theta_0 - \frac{\gamma\mu}{6}\theta_{1s} + \frac{\gamma}{2}\left(\frac{1}{5} + \frac{\mu^2}{6}\right)\theta_t \\ + \frac{\gamma}{6}\lambda + \frac{\gamma\mu}{12}\left(\frac{p_H}{\Omega} \cos \beta_w + \frac{q_H}{\Omega} \sin \beta_w\right) \\ -2\left(\frac{p_H}{\Omega} \cos \beta_w + \frac{q_H}{\Omega} \sin \beta_w\right) + \frac{\gamma}{2}\left(\frac{1}{4} + \frac{\mu^2}{4}\right)\theta_{1c} \\ + \frac{\gamma}{8}\left(\frac{p_H}{\Omega} \sin \beta_w - \frac{q_H}{\Omega} \cos \beta_w\right) \\ -2\left(\frac{p_H}{\Omega} \sin \beta_w - \frac{q_H}{\Omega} \cos \beta_w\right) - \frac{\gamma\mu}{3}\theta_0 \\ - \frac{\gamma\mu}{4}\theta_t + \frac{\gamma}{2}\left(\frac{1}{4} + \frac{3\mu^2}{8}\right)\theta_{1s} \\ - \frac{\gamma\mu}{4}\lambda - \frac{\gamma}{8}\left(\frac{p_H}{\Omega} \cos \beta_w - \frac{q_H}{\Omega} \sin \beta_w\right) \end{bmatrix} \quad (2.15)$$

A notable observation can be made from the above equation on the flapping response due to body angular rates. When the rotor is at hover and under zero roll and pitch controls, the steady state response of β_{1s} and β_{1c} are

$$\beta_{1s} = -\frac{16}{\gamma} \frac{p_H}{\Omega} - \frac{q_H}{\Omega} \quad (2.16)$$

$$\beta_{1c} = \frac{p_H}{\Omega} - \frac{16}{\gamma} \frac{q_H}{\Omega} \quad (2.17)$$

This demonstrates that rotor first harmonic variation of flapping angles is proportional to angular rates of the body during steady pull-up or steady roll flight.

A second simplification involves steady state response of (2.9). In this case, let both first and second derivatives of three blade flapping terms be zero, as follows:

$$K \begin{bmatrix} \beta_0 \\ \beta_{1c} \\ \beta_{1s} \end{bmatrix} = F \quad (2.18)$$

where matrices K and F are from (2.11) and (2.12). For studies that focus on low frequency, (2.18) is more commonly used. Equation (2.18) may not be sufficient for studies involving high fidelity dynamic response validation and aeroelastic analysis.

In a third simplification, steady state response of β_0 , β_{1c} , and β_{1s} are derived from (2.15) for the rotor having zero hinge offset, no flap spring and no pitch-flap coupling, and under zero angular rates;

$$\beta_0 = -\frac{M_\beta}{I_\beta \Omega^2} + \gamma \left[\frac{\theta_0}{8}(1 + \mu^2) + \frac{\theta_t}{10} \left(1 + \frac{5}{6}\mu^2 \right) + \frac{\lambda}{6} - \frac{\mu}{6}\theta_{1s} \right] \quad (2.19)$$

$$\beta_{1s} = \frac{\frac{\mu}{6}\beta_0 + \frac{1}{8}(1 + \mu^2)\theta_{1c}}{\frac{1}{8}(1 + \frac{\mu^2}{2})} \quad (2.20)$$

$$\beta_{1c} = \frac{\frac{\mu}{3}\theta_0 + \frac{\mu}{4}\theta_t + \frac{\mu}{4}\lambda - \frac{1}{8}(1 + \frac{3}{2}\mu^2)\theta_{1s}}{\frac{1}{8}(1 - \frac{\mu^2}{2})} \quad (2.21)$$

At hover, the steady state responses of longitudinal and lateral flapping to the cyclic control inputs can be reduced even further:

$$\beta_{1s} = \theta_{1c} \quad (2.22)$$

$$\beta_{1c} = -\theta_{1s} \quad (2.23)$$

This shows the one-to-one correspondence between the first harmonic flapping and their corresponding cyclic controls.

In the last simplification, it should be noted that for many types of helicopters, their rotor structure is teetering configuration. For teetering configuration, the angle β_0 is treated as a constant pre-cone angle, β_{0p} . It thus follows that $\ddot{\beta}_0 = \dot{\beta}_0 = 0$. The two first harmonic terms β_{1c} and β_{1s} can be solved using two formulae in (2.9):

$$\begin{aligned} & \begin{bmatrix} \ddot{\beta}_{1c} \\ \ddot{\beta}_{1s} \end{bmatrix} + \Omega \begin{bmatrix} \frac{\gamma}{8} & 2 \\ -2 & \frac{\gamma}{8} \end{bmatrix} \begin{bmatrix} \dot{\beta}_{1c} \\ \dot{\beta}_{1s} \end{bmatrix} \\ & + \Omega^2 \begin{bmatrix} P^2 - 1 + \frac{\gamma K_1 \mu^2}{16} & \frac{\gamma}{8} (1 + \frac{\mu^2}{2}) \\ -\frac{\gamma}{8} (1 - \frac{\mu^2}{2}) & P^2 - 1 + \frac{3}{16} \gamma K_1 \mu^2 \end{bmatrix} \begin{bmatrix} \beta_{1c} \\ \beta_{1s} \end{bmatrix} \\ & = \Omega^2 \begin{bmatrix} \frac{\gamma \mu}{6} \\ \frac{\gamma K_1 \mu}{3} \end{bmatrix} \beta_{0p} + \Omega^2 \begin{bmatrix} 0 & 0 \\ -\frac{\gamma \mu}{3} & -\frac{\gamma \mu}{4} \end{bmatrix} \begin{bmatrix} \theta_0 \\ \theta_t \end{bmatrix} \\ & + \Omega^2 \begin{bmatrix} 0 \\ -\frac{\gamma \mu}{4} \end{bmatrix} \lambda + \Omega^2 \begin{bmatrix} \frac{\gamma}{8} (1 + \frac{\mu^2}{2}) & 0 \\ 0 & \frac{\gamma}{8} (1 + \frac{3}{2} \mu^2) \end{bmatrix} \begin{bmatrix} \theta_{1c} \\ \theta_{1s} \end{bmatrix} \\ & + \Omega \begin{bmatrix} -2 & -\frac{\gamma}{8} \\ -\frac{\gamma}{8} & 2 \end{bmatrix} \begin{bmatrix} p_H \cos \beta_w + q_H \sin \beta_w \\ p_H \sin \beta_w - q_H \cos \beta_w \end{bmatrix} \end{aligned} \quad (2.24)$$

2.3.4 Inflow Dynamics

Induced velocity at the rotor can be derived from Momentum Theory. The formulation is represented as rotor inflow ratio λ :

$$\lambda = \frac{w_H}{\Omega R} - \frac{C_T}{2\sqrt{\mu^2 + \lambda^2}} \quad (2.25)$$

When $\mu = 0$, λ can be solved directly from the equation. When $\mu \neq 0$, λ needs to be solved implicitly through the Newton–Raphson iterative technique.

Equation (2.25) is valid when the rotor operates under hover, climb, steep descent, and forward flight conditions. It is not valid under moderate descent rate with slow forward speed when vortex ring state (VRS) occurs. In VRS, the rotor encounters its own wake resulting in a doughnut-shaped ring around the rotor disk. Typical phenomena associated with VRS include flow unsteadiness, excessive thrust and torque fluctuations, uncommanded drop in descent rate, an increase in required power, loss of control effectiveness, and a significant increase in vibration.

One drawback from Momentum Theory is its ignorance of flow interaction between the rotor wake and surrounding airflow in descending condition [44]. Effects of the interaction may be less significant at hover or in climb. Nevertheless, as a rotor increases its descent rate, the interaction becomes more and more intense due to larger velocity gradients between the upflow outside the wake and the downflow inside the wake. As such, a new inflow model was proposed to take into account the flow interactions, known as ring vortex model [13, 15]. The ring vortex model supposes that, due to the flow interaction, there exists a series of vortex rings located at the rotor periphery. Vortex rings move downward along the wake when descending at a low rate. As the rate of descent increases, vortex rings tend to accumulate near the rotor tip. When the rate of descent further increases, vortex rings move upward along the wake. A new vortex ring is formed at every blade rotation, i.e., $\frac{2\pi}{\Omega N_b}$ second. The convection speed of the vortex rings, V_{con} , is approximated as follows:

$$V_{\text{con}} = V_i - \frac{5}{3}w_H \quad (2.26)$$

where the induced velocity $V_i = \frac{C_T}{2\sqrt{(\mu^2 + \lambda^2)}}\Omega R$. The locations of these discrete vortex rings can thus be determined by the product of convection velocity of the vortex rings and $\frac{2m}{\Omega N_b}$ (m : an integer representing the numbering of vortex rings).

Each vortex ring induces additional normal velocity at the rotor disk. The vortex strength of each ring, Γ , is approximated as follows:

$$\Gamma = k_\Gamma V_i R \quad (2.27)$$

where $N_{\text{ring}}k_\Gamma = 0.2167$. The number of vortex rings, N_{ring} , is typically set to two. The flow field of a vortex ring can thus be computed based on elliptic integrals

[12]. One advantage of utilizing vortex rings is that the effect of vortex rings is non-uniform with respect to relative distance between the rings and the rotor disk. The closer a vortex ring is to the rotor disk, the larger the magnitude of normal velocity at the disk. The resulting non-uniform effect conforms to what has been observed in test data.

In the ring vortex model, downward velocity due to vortex rings is integrated into the induced velocity calculated by Momentum Theory. The concept works well in the VRS and windmill phases. Nevertheless, in axial descent and inclined descent at low forward speed ($\frac{\mu}{\sqrt{C_T/2}}$ up to 0.6204), Momentum Theory fails to predict a transition phase between the helicopter and the windmill branches. To address this problem, (2.25) is modified as

$$\lambda = \frac{w_H}{\Omega R} - \frac{C_T}{2\sqrt{k_{RVM}^2 + \mu^2 + \lambda^2}} \quad (2.28)$$

where

$$k_{RVM} = \frac{\lambda}{2.72(1 + \frac{\mu^2}{C_T/2})} \quad (2.29)$$

The additional term k_{RVM} is analogous to the parachute drag term and it modifies equilibrium curves for inflow dynamics, creating a steady state transition between helicopter and windmill branches in axial and steep descents. Its effect diminishes at other flight conditions.

To demonstrate the effectiveness of the ring vortex model, comparison are made between the numerical predictions and wind-tunnel test results from [108] in terms of induced velocity variation (normalized by hover induced velocity, V_h). It is shown from Fig. 2.3 that good agreement is reached with respect to various descent angles α_D .

2.3.5 Main Rotor Forces and Moments

Main rotor forces and moments are calculated in the hub-wind axes system. The quantities include rotor thrust T , H-force H_w , Y-force Y_w , rolling moment L_w , pitching moment M_w , and rotor torque Q .

A closed-form thrust equation is thus provided in the hub-wind axes system [97]:

$$\begin{aligned} T = \frac{n_b}{2} \rho a c R (\Omega R)^2 \left\{ \frac{1}{2} (1 - \epsilon^2) \lambda + \theta_0 \left[\frac{1}{3} + \frac{\mu^2}{2} (1 - \epsilon) \right] + \theta_t \left[\frac{1}{4} + \frac{\mu^2}{4} (1 - \epsilon^2) \right] \right. \\ \left. - \frac{\mu}{2} (1 - \epsilon^2) (\theta_{1s} - K_1 \beta_{1s}) - \beta_0 \left[\frac{1}{3} + \frac{\mu^2}{2} (1 - \epsilon) \right] K_1 + \beta_{1c} \left[\frac{\mu}{2} \epsilon (1 - \epsilon) \right] \right\} \end{aligned} \quad (2.30)$$

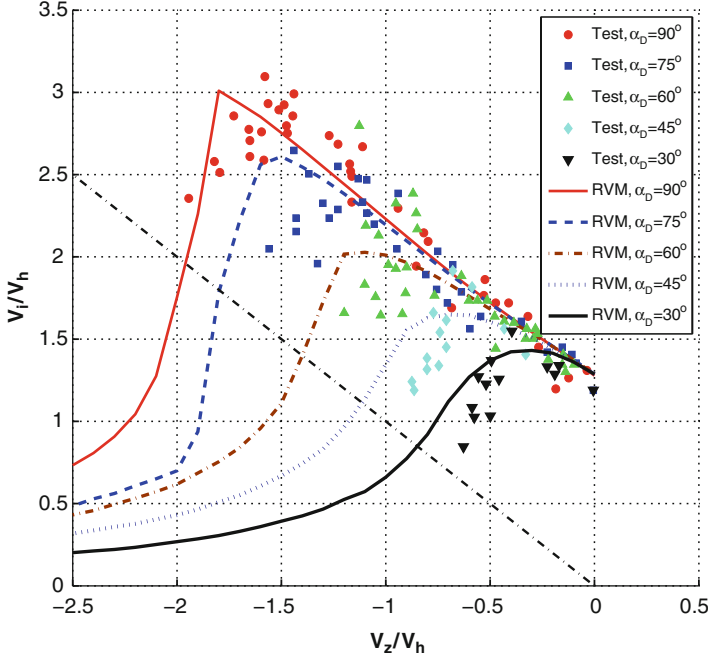


Fig. 2.3 Induced velocity variations from Yaggy's wind-tunnel test [108] and predictions from the ring vortex model: axial and nonaxial flow

In many hobby helicopter models, their blades are teetering ($\epsilon = 0$), have untwisted blades ($\theta_t = 0$), and are without pitch flap coupling ($K_1 = 0$). The thrust equation can thus be further simplified as:

$$T = \frac{n_b}{2} \rho a c R (\Omega R)^2 \left\{ \frac{\lambda}{2} + \theta_0 \left[\frac{1}{3} + \frac{\mu^2}{2} \right] - \frac{\mu}{2} \theta_{1s} \right\} \quad (2.31)$$

Horizontal force component H_w is provided [97] as

$$\begin{aligned} H_w = & \frac{n_b}{2} \rho a c R (\Omega R)^2 \left\{ \frac{\delta \mu}{2a} (1 - \epsilon^2) \right. \\ & - \frac{1}{4} (\theta_0 - K_1 \beta_0) \left[2\lambda \mu (1 - \epsilon) + \left(\epsilon - \frac{2}{3} \right) \beta_{1c} - \frac{2}{3} \beta_{1c} \right] \\ & - \frac{\theta_t}{4} \left[\mu \lambda (1 - \epsilon^2) + 2 \left(\frac{\epsilon}{3} - \frac{1}{4} \right) \beta_{1c} - \frac{\beta_{1c}}{2} \right] \\ & \left. + \frac{1}{4} (\theta_{1c} - K_1 \beta_{1c}) \left[-\frac{\beta_{1s} \mu}{4} (1 - \epsilon^2) + \frac{1}{4} \mu (1 - \epsilon)^2 \beta_{1s} + \frac{2}{3} \beta_0 \right] \right\} \end{aligned}$$

$$\begin{aligned}
& + \frac{1}{4}(\theta_{1s} - K_1\beta_{1s}) \left[-\frac{3}{4}\mu(1-\epsilon)^2\beta_{1c} + (1-\epsilon^2) \left(\lambda - \frac{\beta_{1c}\mu}{4} \right) \right] \\
& + \frac{1}{4} \left[-4\epsilon(1-\epsilon)\beta_{1c}\lambda - 3(1-\epsilon^2)\lambda\beta_{1c} - \left(\frac{2}{3} - \epsilon \right) \beta_0\beta_{1s} \right] \\
& + \frac{\mu}{4} \left[\epsilon(1-\epsilon)(-\beta_{1c}^2 + \beta_{1s}^2) + \frac{1}{4}(1-\epsilon)^2(-\beta_{1c}^2 + \beta_{1s}^2) \right. \\
& \left. - \frac{1}{2}(1-\epsilon^2) \left(-2\beta_0^2 - \frac{5}{2}\beta_{1c}^2 + \frac{1}{2}\beta_{1s}^2 \right) \right] \Big\} \quad (2.32)
\end{aligned}$$

where the equivalent rotor blade profile drag coefficient, δ , is defined as

$$\delta = 0.009 + 0.3 \left(\frac{6C_T}{\sigma a} \right)^2 \quad (2.33)$$

Note that the term $\frac{6C_T}{\sigma a}$ is also known as averaged blade angle of attack. Therefore, (2.33) is the second order approximation for computing blade drag coefficient based on averaged angle of attack.

Similarly, the side-force component Y_w is given [97] as

$$\begin{aligned}
Y_w = & \frac{n_b}{2} \rho a c R (\Omega R)^2 \left(-\frac{1}{4}(\theta_0 - K_1\beta_0) \left[\left(\epsilon - \frac{2}{3} \right) \beta_{1s} \right. \right. \\
& \left. \left. - \frac{2}{3}\beta_{1s} + 3\beta_0(1-\epsilon^2)\mu - 2\beta_{1s}(1-\epsilon)\mu^2 \right] \right. \\
& \left. - \frac{\theta_t}{4} \left[\left(\frac{2}{3}\epsilon - \frac{1}{2} \right) \beta_{1s} - \frac{\beta_{1s}}{2} + 2\beta_0\mu - \beta_{1s}(1-\epsilon^2)\mu^2 \right] \right. \\
& \left. - \frac{1}{4}(\theta_{1c} - K_1\beta_{1c}) \left\{ \lambda(1-\epsilon^2) + \mu \left[\frac{5}{4}\beta_{1c}(1-\epsilon^2) - \frac{1}{4}(1-\epsilon)^2\beta_{1c} \right] \right\} \right. \\
& \left. - \frac{1}{4}(\theta_{1s} - K_1\beta_{1s}) \left[-\frac{2}{3}\beta_0 + \mu \left(\frac{7}{4}\beta_{1s}(1-\epsilon^2) + \frac{1}{4}(1-\epsilon)^2\beta_{1s} \right) \right. \right. \\
& \left. \left. - 2\beta_0\mu^2(1-\epsilon) \right] - \frac{1}{4} \left[-2\lambda(1-\epsilon)^2\beta_{1s} - 2\beta_0\beta_{1c} \left(\frac{1}{3} - \frac{\epsilon}{2} \right) - \lambda\beta_{1s}(1-\epsilon^2) \right] \right. \\
& \left. - \frac{\mu}{4} \left[6\beta_0\lambda(1-\epsilon) - \frac{1}{2}\beta_{1c}\beta_{1s}(1-\epsilon^2) - \frac{7}{4}(1-\epsilon)^2\beta_{1c}\beta_{1s} \right. \right. \\
& \left. \left. + \frac{5}{4}(1-\epsilon)^2\beta_{1c}\beta_{1s} \right] - \mu^2\beta_0\beta_{1c}(1-\epsilon) \right) \quad (2.34)
\end{aligned}$$

The calculated rotor forces are transformed back from hub-wind axes system to hub axes system:

$$\begin{bmatrix} H_H \\ Y_H \\ T \end{bmatrix} = \begin{bmatrix} \cos \beta_w & \sin \beta_w & 0 \\ -\sin \beta_w & \cos \beta_w & 0 \\ 0 & 0 & 1 \end{bmatrix} \begin{bmatrix} H_w \\ Y_w \\ T \end{bmatrix} \quad (2.35)$$

Rolling moment L_w is computed based on the following formula [97]:

$$\begin{aligned} L_w = & \frac{n_b}{2} \left(k_\beta \beta_{1s} + \frac{eM_\beta}{g} \beta_{1s} \Omega^2 \right) - \frac{n_b}{2} I_\beta \Omega^2 \gamma \epsilon \left\{ \frac{\mu}{2} (1 - \epsilon^2) (\theta_0 - K_1 \beta_0) \right. \\ & - \left[\frac{1}{6} + \frac{3}{8} \mu^2 (1 - \epsilon) \right] (\theta_{1s} - K_1 \beta_{1s}) + \frac{\mu}{3} \theta_t + \frac{\mu}{2} (1 - \epsilon) \lambda \\ & \left. + \frac{\mu^2}{8} (1 - \epsilon) \beta_{1c} - \left(\frac{1}{6} - \frac{\epsilon}{4} \right) \beta_{1c} \right\} \end{aligned} \quad (2.36)$$

Similarly, pitching moment M_w is calculated [97] as

$$\begin{aligned} M_w = & \frac{n_b}{2} \left(k_\beta \beta_{1c} + \frac{eM_\beta}{g} \beta_{1c} \Omega^2 \right) \\ & - \frac{n_b}{2} I_\beta \Omega^2 \gamma \epsilon \left\{ - \left[\frac{1}{6} + \frac{\mu^2}{8} (1 - \epsilon) \right] (\theta_{1c} - K_1 \beta_{1c}) \right. \\ & \left. - \frac{\mu}{4} (1 - \epsilon^2) \beta_0 + \frac{\mu^2}{8} (1 - \epsilon) \beta_{1s} + \left(\frac{1}{6} - \frac{\epsilon}{4} \right) \beta_{1s} \right\} \end{aligned} \quad (2.37)$$

For helicopter rotors with teetering blades and no flapping spring constraint, it follows that $L_w = 0$ and $M_w = 0$. It is also interesting to study rotor blades with hinge offset and/or flapping spring constraint. In this case, let $C_{L_w} = L_w / (\rho A R (\Omega R)^2)$ and $C_{M_w} = M_w / (\rho A R (\Omega R)^2)$ be coefficients of rolling moment and pitching moment, respectively. From both (2.36) and (2.37), it results in:

$$C_{L_w} = \frac{\sigma a}{2} \frac{P^2 - 1}{\gamma} \beta_{1s} \quad (2.38)$$

$$C_{M_w} = \frac{\sigma a}{2} \frac{P^2 - 1}{\gamma} \beta_{1c} \quad (2.39)$$

Recall that P is known as the non-dimensional flap frequency. This demonstrates that for a rotor with hinge offset or flap spring, the direct hub rolling and pitching moments are proportional to rotor first-harmonic tilting. As for the resultant rolling and pitching moments acting on the vehicle's C.G., they are the summation of direct hub moment and the moments caused by the tilting of the rotor thrust about the body's C.G. For an articulated rotor, direct hub moments are about the same

as the moments from the thrust tilting. For a hingeless or rigid rotor, the direct hub moments may be two to four times larger than the moments from the thrust tilting.

Main rotor torque can either be estimated from rotor power consumption (as will be illustrated in Sect. 2.4), or from the closed-form expression given as follows [97]:

$$\begin{aligned}
 Q = \frac{n_b}{2} \rho a c R^2 (\Omega R)^2 \left\{ \frac{\delta}{4a} [1 + (1 - \epsilon^2)\mu^2] - (\theta_0 - K_1\beta_0) \left(\frac{\lambda}{3} + \frac{\mu}{4}\epsilon\beta_{1c} \right) \right. \\
 + (\theta_{1c} - K_1\beta_{1c}) \left[\left(\frac{1}{8} - \frac{\epsilon}{6} \right) \beta_{1s} - \frac{\mu}{6}\beta_0 - \frac{\beta_{1s}}{16}(1 - \epsilon^2)\mu^2 \right] \\
 + (\theta_{1s} - K_1\beta_{1s}) \left[- \left(\frac{1}{8} - \frac{\epsilon}{6} \right) \beta_{1c} + \frac{1}{2}(1 - \epsilon^2) \left(\frac{\mu\lambda}{2} + \frac{\beta_{1c}}{8}\mu^2 \right) \right] \\
 - \theta_t \left(\frac{\lambda}{4} + \frac{\epsilon\mu}{6}\beta_{1c} \right) - \frac{1}{2}(1 - \epsilon^2) \left[\lambda^2 + \lambda\mu\beta_{1c} + \mu\epsilon\beta_0\beta_{1s} + \mu^2 \left(\frac{\beta_0^2}{2} + \frac{3}{8}\beta_{1c}^2 \right. \right. \\
 \left. \left. + \frac{1}{8}\beta_{1s}^2 \right) \right] + \frac{\mu}{3}\beta_0\beta_{1s} - \left(\frac{1}{4} - \frac{2}{3}\epsilon + \frac{\epsilon^2}{2} \right) \left(\frac{1}{2}\beta_{1s}^2 + \frac{1}{2}\beta_{1c}^2 \right) \left. \right\} \quad (2.40)
 \end{aligned}$$

The calculated rotor moments are transformed from the hub-wind axes system back to the hub axes system:

$$\begin{bmatrix} L_H \\ M_H \\ Q \end{bmatrix} = \begin{bmatrix} \cos \beta_w & -\sin \beta_w & 0 \\ \sin \beta_w & \cos \beta_w & 0 \\ 0 & 0 & 1 \end{bmatrix} \begin{bmatrix} L_w \\ M_w \\ Q \end{bmatrix} \quad (2.41)$$

2.3.6 Transformation from Hub to Body

The forces at the rotor hub are further transformed into the body axes system involving the forward tilting of the rotor shaft i_s :

$$\begin{bmatrix} X_{MR} \\ Y_{MR} \\ Z_{MR} \end{bmatrix} = \begin{bmatrix} \cos i_s & 0 & -\sin i_s \\ 0 & 1 & 0 \\ \sin i_s & 0 & \cos i_s \end{bmatrix} \begin{bmatrix} -H_H \\ Y_H \\ -T \end{bmatrix} \quad (2.42)$$

Similarly, the moments at the rotor hub are transformed back to the body axes system, involving the forward tilting of the rotor shaft as well as additional moments about the C.G. from the rotor forces due to spatial separation between the C.G. and the rotor hub:

$$\begin{bmatrix} L_{MR} \\ M_{MR} \\ N_{MR} \end{bmatrix} = \begin{bmatrix} \cos i_s & 0 & -\sin i_s \\ 0 & 1 & 0 \\ \sin i_s & 0 & \cos i_s \end{bmatrix} \begin{bmatrix} L_H \\ M_H \\ Q \end{bmatrix} - \begin{bmatrix} STA_H - STA_{CG} \\ BL_H - BL_{CG} \\ WL_H - WL_{CG} \end{bmatrix} \times \begin{bmatrix} X_{MR} \\ Y_{MR} \\ Z_{MR} \end{bmatrix} \quad (2.43)$$

2.3.7 Tail Rotor

A tail rotor usually serves two purposes for a conventional single main-rotor helicopter: to provide anti-torque for the main rotor and to support directional control.

The analysis of a tail rotor is very similar to that of a main rotor [97]. In fact, it is often treated as a special case of the main rotor in terms of both flapping and force calculations. However, there are some special features associated with the tail rotor which may make the analysis easier. These features include:

- The tail rotor has only collective for the thrust, and hence there is no cyclic pitch control ($\theta_{1c} = \theta_{1s} = 0$);
- The tail rotor rotates at a much faster speed, hence a steady state blade flapping response in the non-rotating frame is sufficient.

The tail rotor may come in various configurations, including teetering, articulated, hingeless, bearingless, Fenestrans (fan-in-fin), and even NOTAR (No Tail Rotor). As the teetering is still the most commonly used configuration, the study in this section will focus on the teetering tail rotor.

As a first step, the velocity components at the body C.G. frame is transformed to the local velocity at the hub of the tail rotor:

$$\begin{bmatrix} u_{TR} \\ v_{TR} \\ w_{TR} \end{bmatrix} = \begin{bmatrix} u_B \\ v_B \\ w_B \end{bmatrix} + \begin{bmatrix} STA_{TR} - STA_{CG} \\ BL_{TR} - BL_{CG} \\ WL_{TR} - WL_{CG} \end{bmatrix} \times \begin{bmatrix} p_B \\ q_B \\ r_B \end{bmatrix} + \begin{bmatrix} 0 \\ 0 \\ w_{iTR} \end{bmatrix} \quad (2.44)$$

where w_{iHT} is the velocity that accounts for the interference from the main rotor to the tail rotor. The advance ratio and sideslip angle for the tail rotor can thus be obtained as

$$\mu_{TR} = \frac{\sqrt{u_{TR}^2 + w_{TR}^2}}{\Omega_{TR} R_{TR}} \quad (2.45)$$

$$\beta_{TR} = \tan^{-1} \left(\frac{w_{TR}}{u_{TR}} \right) \quad (2.46)$$

Since a steady state solution is sufficient for the teetering tail rotor, it follows that $\ddot{\beta}_{1c} = \ddot{\beta}_{1s} = \dot{\beta}_{1c} = \dot{\beta}_{1s} = 0$. The two first harmonic terms β_{1c} and β_{1s} can be solved by using (2.24). Notice that $\theta_{1c} = \theta_{1s} = 0$ in the case of a tail rotor. The inflow ratio for the tail rotor is very similar to that for the main rotor:

$$\lambda_{TR} = -\frac{v_{TR}}{\Omega_{TR} R_{TR}} - \frac{C_{T_{TR}}}{2\sqrt{\mu_{TR}^2 + \lambda_{TR}^2}} \quad (2.47)$$

For the tail rotor thrust, H-force, and Y-force, (2.30), (2.32), and (2.34) can be applied by selecting corresponding tail rotor parameters and setting $\epsilon = 0$. As mentioned earlier, the rolling and pitching moments of the tail rotor are zero due to its teetering configuration. For the tail rotor torque, (2.40) can be applied.

All forces and moments for the tail rotor are transformed back from the hub wind frame to body frame:

$$\begin{bmatrix} X_{TR} \\ Y_{TR} \\ Z_{TR} \end{bmatrix} = \begin{bmatrix} \cos \beta_{TR} & -\sin \beta_{TR} & 0 \\ 0 & 0 & 1 \\ \sin \beta_{TR} & \cos \beta_{TR} & 0 \end{bmatrix} \begin{bmatrix} -H_{wTR} \\ Y_{wTR} \\ T_{TR} \end{bmatrix} \quad (2.48)$$

$$\begin{bmatrix} L_{TR} \\ M_{TR} \\ N_{TR} \end{bmatrix} = \begin{bmatrix} 0 \\ -Q_{TR} \\ 0 \end{bmatrix} - \begin{bmatrix} STA_{TR} - STA_{CG} \\ BL_{TR} - BL_{CG} \\ WL_{TR} - WL_{CG} \end{bmatrix} \times \begin{bmatrix} X_{TR} \\ Y_{TR} \\ Z_{TR} \end{bmatrix} \quad (2.49)$$

2.3.8 Propeller

The analysis of a propeller is very similar to a helicopter rotor. In fact, the basic analytical tools are the same: Momentum theory and Blade Element theory. However, caution must be taken when applying closed-form equations in Sect. 2.3.1 to the propeller performance calculation. This is because a few assumptions in reaching the closed-form equations are no longer valid. For example, it is common that a propeller blade can have fairly large pitch, in which case we can not make a small angle assumption. Moreover, the chordwise blade profile can be much more complicated than that of an ordinary rotor blade.

A propeller thrust and torque calculation procedure (based on Vortex theory [68]) will be provided in the following sections. Historically, the terminology used in the helicopter rotor and the propeller are quite different. For example, the advance ratio for the helicopter rotor is defined as $\frac{V}{\Omega R}$, while the same term for the propellers is defined as $\frac{V}{nD} = \frac{\pi V}{\Omega R}$ (n is the rotational speed in revolutions per second and D is the propeller diameter). The procedure will adopt the typical nomenclature from helicopter theory books.

1. Break a single propeller blade into n elements. Let r and x be the collection of dimensional and dimensionless radial stations along the blade.
2. Let w_t and w_a be tangential and axial components of the induced velocity. Assume $\frac{w_t}{V_T} = 0$, where $V_T = \Omega R$ is the tip velocity of the propeller blade.
3. Calculate w_a :

$$\frac{w_a}{V_T} = \frac{1}{2} \left[-\mu + \sqrt{\mu^2 + 4 \frac{w_t}{V_T} \left(x - \frac{w_t}{V_T} \right)} \right] \quad (2.50)$$

where $\mu = \frac{V}{V_T}$ is the advance ratio for the propeller.

4. Obtain $\phi = \tan^{-1} \frac{\mu}{x}$.
5. Calculate induced angle of attack α_i :

$$\alpha_i = \tan^{-1} \left(\frac{V + w_a}{\Omega r - w_t} \right) - \phi \quad (2.51)$$

6. Compute a correction term for finite thickness of the blade:

$$\Delta\alpha = \frac{4\mu\sigma}{15(\mu^2 + x^2)} \frac{t_{\max}}{c} \quad (2.52)$$

where t_{\max} is the maximum thickness of the blade and c is the sectional blade chord.

7. Obtain local angle of attack:

$$\alpha = \theta - \alpha_i - \phi - \Delta\alpha \quad (2.53)$$

8. Compute a second correction term for effective camber due to flow curvature:

$$\Delta C_l = \frac{a\Delta\theta}{4} \quad (2.54)$$

where $\Delta\theta = \tan^{-1} \left(\frac{V + w_a}{\Omega r - 2w_t} \right) - \tan^{-1} \left(\frac{V + w_a}{\Omega r} \right)$.

9. Obtain sectional lift coefficient C_l :

$$C_l = a(\alpha + \alpha_{0l}) - \Delta C_l \quad (2.55)$$

where α_{0l} is the angle between the zero-lift line and the chord line for the propeller airfoil.

10. Calculate sectional total velocity V_e :

$$\frac{V_e}{V_T} = \sqrt{\left(\mu + \frac{w_a}{V_T} \right)^2 + \left(x - \frac{w_t}{V_T} \right)^2} \quad (2.56)$$

11. Obtain bound circulation Γ :

$$\Gamma = \frac{1}{2} v C_l V_e \quad (2.57)$$

12. Update w_t :

$$w_t = \frac{n_b \Gamma}{4\pi r F} \quad (2.58)$$

where F is the Prandtl's tip loss factor

$$F = \frac{2}{\pi} \cos^{-1} \exp \left[-\frac{n_b(1-x)}{2 \sin \theta_T} \right] \quad (2.59)$$

13. Return to Step 3 until the absolute difference (vector norm) between the calculated w_t and that from the previous calculation reduces to a desired value.
14. Obtain differential lift dL and differential drag dD :

$$dL = \frac{1}{2} \rho V_e^2 c C_l dr \quad (2.60)$$

$$dD = \frac{1}{2} \rho V_e^2 c C_d dr \quad (2.61)$$

where sectional drag coefficient C_d can be represented as a function of C_l .

15. Compute sectional thrust dT and torque dQ :

$$dT = dL \cos(\phi + \alpha_i) - dD \sin(\phi + \alpha_i) \quad (2.62)$$

$$dQ = r[dL \sin(\phi + \alpha_i) + dD \cos(\phi + \alpha_i)] \quad (2.63)$$

16. Numerically integrate the above two equations in order to obtain the total thrust T and torque Q .
17. Finally, compute the propeller efficiency:

$$\eta = \frac{TV}{Q\Omega} \quad (2.64)$$

The procedure listed above is used to compute thrust and power for a three-bladed propeller with Clark-Y section from a wind-tunnel test [37]. The predicted non-dimensional thrust and torque coefficients from Vortex Theory are compared with the experimental results in Fig. 2.4 for two different blade pitch angles at 0.75R: 15° and 35°. The prediction clearly matches with the test very well. In addition, another set of predictions using combined Momentum-Blade Element Theory is also provided (for computational procedure with this method, refer to [68]). Prediction with Vortex Theory is considerably precise as it takes into account flow rotation, tip loss, finite thickness of a blade, and effective camber of the blade section due to flow curvature.

2.3.9 Horizontal Tail

In steady forward flight, the horizontal tail can generate a trim load to compensate main rotor longitudinal flapping [97]. More importantly, the horizontal tail is able

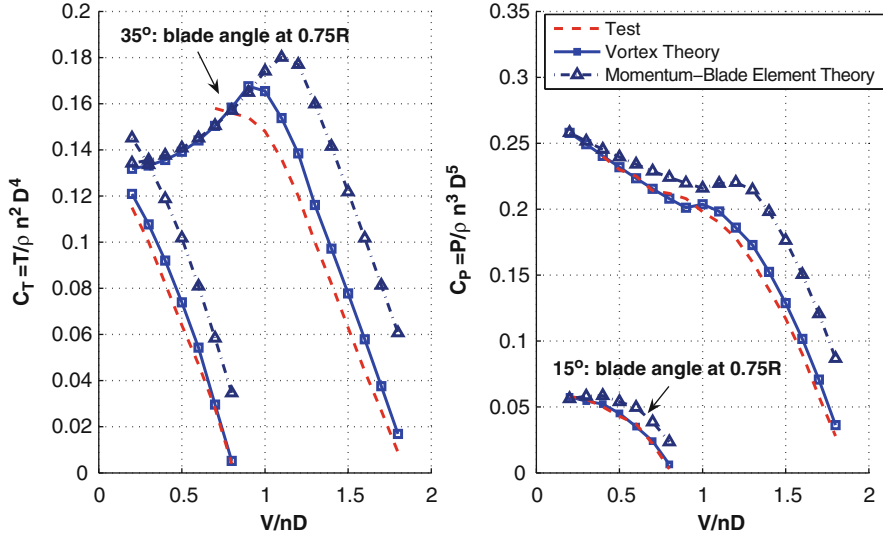


Fig. 2.4 Comparison of predictions from Vortex Theory and Momentum-Blade Element Theory with experiment from [37]

to provide a stabilizing pitch moment due to angle of attack variation to enhance the pitch stability. Primary forces from the horizontal tail are lift and drag.

The velocity components acting on the horizontal tail in its local body axes system are as follows:

$$\begin{bmatrix} u_{HT} \\ v_{HT} \\ w_{HT} \end{bmatrix} = \begin{bmatrix} u_B \\ v_B \\ w_B \end{bmatrix} + \begin{bmatrix} STA_{HT} - STA_{CG} \\ BL_{HT} - BL_{CG} \\ WL_{HT} - WL_{CG} \end{bmatrix} \times \begin{bmatrix} p_B \\ q_B \\ r_B \end{bmatrix} + \begin{bmatrix} 0 \\ 0 \\ w_{iHT} \end{bmatrix} \quad (2.65)$$

where w_{iHT} is the velocity that accounts for the interference angle from the main rotor to the horizontal tail. The angle of attack and sideslip angle of the horizontal tail are then obtained:

$$\alpha_{HT} = \tan^{-1} \left(\frac{w_{HT}}{u_{HT}} \right) + i_{HT} \quad (2.66)$$

$$\beta_{HT} = \sin^{-1} \left(\frac{v_{HT}}{V_{HT}} \right) \quad (2.67)$$

where

$$V_{HT} = \sqrt{u_{HT}^2 + v_{HT}^2 + w_{HT}^2} \quad (2.68)$$

and the angle i_{HT} is the incidence of the horizontal tail. For a cambered airfoil, i_{HT} is adjusted to include the angle of attack for zero-lift. For a movable horizontal tail, i_{HT} can be used as a trim variable, like an elevator for a fixed-wing aircraft.

Lift and drag on the horizontal tail can then be calculated in the local wind axis system using quadratic aerodynamic form for airfoils:

$$L_{HT} = \frac{1}{2} \rho V_{HT}^2 S_{HT} C_{L_{HT}} \quad (2.69)$$

$$D_{HT} = \frac{1}{2} \rho V_{HT}^2 S_{HT} C_{D_{HT}} \quad (2.70)$$

Full range lift coefficient $C_{L_{HT}}$ and drag coefficient $C_{D_{HT}}$ for certain airfoils are available from the airfoil database from the Department of Aerospace Engineering, University of Illinois at Urbana-Champaign. A simplified version is provided [44]:

$$C_{L_{HT}} = a \alpha_{HT} \quad (2.71)$$

$$C_{D_{HT}} = 0.0087 - 0.0216 \alpha_{HT} + 0.4 \alpha_{HT}^2 \quad (2.72)$$

where a is the lift curve slope, and $C_{D_{HT}}$ is obtained for the NACA 23012 airfoil and considered accurate up to its stall angle (12°).

Subsequently, lift and drag can be transformed from local wind axes system to local body axes system:

$$\begin{bmatrix} X_{HT} \\ Y_{HT} \\ Z_{HT} \end{bmatrix} = \begin{bmatrix} \cos \alpha_{HT} & 0 & -\sin \alpha_{HT} \\ 0 & 1 & 0 \\ \sin \alpha_{HT} & 0 & \cos \alpha_{HT} \end{bmatrix} \begin{bmatrix} \cos \beta_{HT} & -\sin \beta_{HT} & 0 \\ \sin \beta_{HT} & \cos \alpha_{HT} & 0 \\ 0 & 0 & 1 \end{bmatrix} \begin{bmatrix} -D_{HT} \\ 0 \\ -L_{HT} \end{bmatrix} \quad (2.73)$$

Moments associated with the horizontal tail are computed based on the location of the aerodynamic center on the tail with respect to the body C.G.:

$$\begin{bmatrix} L_{HT} \\ M_{HT} \\ N_{HT} \end{bmatrix} = - \begin{bmatrix} STA_{HT} - STA_{CG} \\ BL_{HT} - BLCG \\ WL_{HT} - WLCG \end{bmatrix} \times \begin{bmatrix} X_{HT} \\ Y_{HT} \\ Z_{HT} \end{bmatrix} \quad (2.74)$$

In general, lift on the horizontal tail is the dominant force while pitch moment is the dominant moment. It, therefore, may be sufficient just to compute the lift and pitch moment from the horizontal tail in certain applications.

2.3.10 Wing

Wing is sometimes added to a rotor-wing aircraft to produce lift during forward flight. The wing is treated in the same manner as the horizontal tail. All the formulae listed in Sect. 2.3.9 are portable in the calculation of forces and moments for the wing module.

2.3.11 Vertical Tail

The vertical tail can be treated in a similar fashion as the horizontal tail with minor differences. In a standard single main rotor configuration, an additional interference effect needs to be taken into account from the tail rotor to the vertical tail [97]. As such, the velocity components acting on the vertical tail in its local body axes system are as follows:

$$\begin{bmatrix} u_{VT} \\ v_{VT} \\ w_{VT} \end{bmatrix} = \begin{bmatrix} u_B \\ v_B \\ w_B \end{bmatrix} + \begin{bmatrix} STA_{VT} - STA_{CG} \\ BL_{VT} - BL_{CG} \\ WL_{VT} - WL_{CG} \end{bmatrix} \times \begin{bmatrix} p_B \\ q_B \\ r_B \end{bmatrix} + \begin{bmatrix} 0 \\ k_{vtr} w_{itr} \\ w_{iVT} \end{bmatrix} \quad (2.75)$$

where w_{iVT} is the interference velocity from the main rotor to the vertical tail. The term w_{itr} accounts for the blockage effect due to the tail rotor. The angle of attack and sideslip angle of the vertical tail are calculated in consideration of different orientations between the horizontal tail and vertical tail:

$$\alpha_{HT} = \tan^{-1} \left(\frac{v_{VT}}{u_{VT}} \right) + i_{VT} \quad (2.76)$$

$$\beta_{HT} = \sin^{-1} \left(\frac{w_{VT}}{V_{VT}} \right) \quad (2.77)$$

where

$$V_{VT} = \sqrt{u_{VT}^2 + v_{VT}^2 + w_{VT}^2} \quad (2.78)$$

and the angle i_{HT} is the incidence angle of the vertical tail. The angle i_{HT} is adjusted to include the angle of attack for zero-lift for cambered airfoil and can be used as a trim variable for movable vertical tail, like a rudder for a fixed-wing aircraft. The remaining calculation of forces and moments for the vertical tail can be directly referred to Sect. 2.3.9.

2.3.12 Fuselage

Aerodynamic forces and moments acting on the fuselage can be computed in almost the exact manner as the horizontal tail. However, one difficulty in the case of the fuselage is the determination of the aerodynamic database. While such database for the horizontal tail is still relatively easy to find due to its airfoil shape, it is generally difficult for the fuselage due to its bluff body shape. Conducting a wind-tunnel experiment or a comprehensive computational study are certainly beneficial, although they may sometimes be costly and time-consuming.

An alternative is to estimate equivalent flat-plate areas for all body-x, body-y, and body-z axes and calculate correspondingly forces along those axes. Similar to the horizontal and vertical tails, the velocity components acting on the fuselage in its local body axes system are [97]:

$$\begin{bmatrix} u_{FU} \\ v_{FU} \\ w_{FU} \end{bmatrix} = \begin{bmatrix} u_B \\ v_B \\ w_B \end{bmatrix} + \begin{bmatrix} 0 \\ 0 \\ w_{iFU} \end{bmatrix} \quad (2.79)$$

where w_{iFU} is the interference velocity from the main rotor to the fuselage. Note that the effects from angular rates are ignored here due to close distance between fuselage aerodynamic center and body C.G. Let S_{Ref}^{front} , S_{Ref}^{side} , and S_{Ref}^{top} be the equivalent flat-plate areas along the body-x, body-y, body-z axes, the forces on the fuselage are

$$\begin{bmatrix} X_{FU} \\ Y_{FU} \\ Z_{FU} \end{bmatrix} = \begin{bmatrix} \frac{1}{2} \rho u_{FU}^2 S_{Ref}^{front} \\ \frac{1}{2} \rho v_{FU}^2 S_{Ref}^{side} \\ \frac{1}{2} \rho w_{FU}^2 S_{Ref}^{top} \end{bmatrix} \quad (2.80)$$

The above forces are assumed to act on the fuselage's center of pressure. A suggestion is provided to relate fuselage frontal drag area with the rest: $S_{Ref}^{side} = 2.2 S_{Ref}^{front}$ and $S_{Ref}^{top} = 1.5 S_{Ref}^{front}$. Moments due to the aerodynamic forces with respect to the body C.G. are

$$\begin{bmatrix} L_{FU} \\ M_{FU} \\ N_{FU} \end{bmatrix} = - \begin{bmatrix} STA_{FU} - STA_{CG} \\ BL_{FU} - STA_{CG} \\ WL_{FU} - WL_{CG} \end{bmatrix} \times \begin{bmatrix} X_{FU} \\ Y_{FU} \\ Z_{FU} \end{bmatrix} \quad (2.81)$$

2.3.13 Aerodynamic Interference

Aerodynamic interference among different modules are essential in rotorcraft modeling. Sometimes the interference introduces power penalties or loss of efficiency. For example, additional vertical loading on the fuselage due to main rotor downwash in hover condition could count for as much as 5% of total weight. In another example, for a tail rotor in pusher configuration, its aerodynamic efficiency decreases due to blackage effect from the vertical tail. The interference can be productive in other cases. For example, a horizontal tail immersed in the main rotor downwash contributes a stabilizing pitch moment for longitudinal static stability. A rudder immersed in a propwash for an autogyro could increase its control effectiveness at low speed.

A typical assumption in dealing with interference is airflow superposition. An additional velocity vector from the source of the interference is superimposed to the resultant module's local velocity vector, thus resulting in changes in local angle of attack and sideslip angle. The superposition method shall be treated as a first-order approximation of the actual interference.

From data presented in [42], an empirical expression for interference velocity w_i due to a rotor was provided in [97]:

$$w_i = k_f v_i \quad (2.82)$$

where v_i is the averaged downwash at the rotor plane. The empirical factor k_f is given as follows:

$$k_f = 1.299 + 0.671\chi - 1.172\chi^2 + 0.351\chi^3 \quad (2.83)$$

where the rotor wake angle χ is defined as

$$\chi = \tan^{-1} \left(\frac{\mu}{-\lambda} \right) \quad (2.84)$$

For convenience, the graphical relationship between the interference factor and the rotor wake angle is provided in Fig. 2.5. The interference velocity in Sects. 2.3.7–2.3.12 can be computed using (2.82).

2.3.14 Rotor Rotational Degree of Freedom

In most rotary-wing flight dynamics modeling, rotor speed is assumed to be constant. This assumption is certainly valid in the presence of a governor module, which is designed to maintain the rotor speed through a feedback system. Nevertheless, for a helicopter operating in auto-rotation mode or an autogyro, the rotor speed is not determined by an engine but rather by the balancing of driving torque and driven

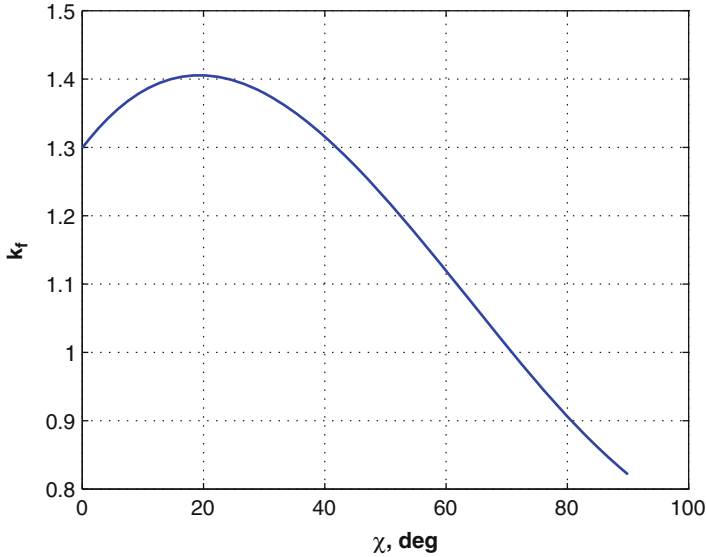


Fig. 2.5 Interference factor with respect to rotor wake angle

torque at the rotor. In such a case, it is necessary to set up rotor rotational degree of freedom. This equation is described as follows:

$$J\dot{\Omega} = -Q \quad (2.85)$$

where Q is the rotor torque. Rotor rotation inertia J can be approximated using the blade flapping inertia I_β :

$$J = N_b I_\beta \quad (2.86)$$

where N_b is the number of blades.

2.3.15 Flight Control System

In general, the flight control module consists of at least one of the following systems:

- Feedforward mechanical system, including pilot's controls, mechanical linkage, actuation system, swashplate, and control rods. This system can normally be represented by linear equations between the pilot's controls and blade pitch variations. It may also include first order transfer functions for actuators and nonlinear saturation representing control limits.

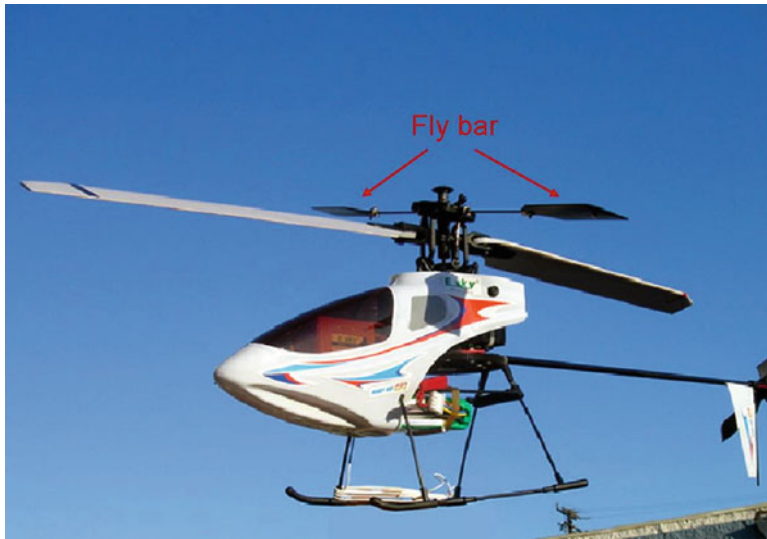


Fig. 2.6 Teetering rotor configuration with a fly bar for a model helicopter

- Automatic flight control system (AFCS), including stability augmentation system (SAS) and control augmentation system (CAS). Details of AFCS design will be illustrated in later chapters.
- Fly bar (also known as stabilizer bar) for teetering rotor configuration (see Fig. 2.6).

The fly bar deserves an in-depth discussion as it is a common feature found in the 2-bladed teetering rotor configuration. The reason is that this type of rotor configuration tends to have excessively rapid response to cyclic controls. The installation of fly bar provides lagged rate feedback to slow down the fast response.

The bar consists essentially of a rod with two small airfoils at two ends. Without cyclic controls, the bar maintains its rotational plane parallel to the ground. With cyclic controls, the bar responds in a manner similar to the main rotor blades. There are historically two types of fly bars: Hiller bar and Bell–Hiller bar. For the Hiller bar, cyclic controls are first transmitted from the rotating swashplate to the bar. Subsequently, cyclic pitch variations of the rotor blades are controlled entirely by the tilting of the bar. For the Bell–Hiller bar, there is a mechanical mixer between the bar and the rotor blades. Cyclic controls go to the bar as in the case of the Hiller bar. However, there is another portion of cyclic controls that go directly to the rotor blades. The tilting of the bar due to the cyclic controls goes further to the rotor blades via the mixer. One advantage of the Bell–Hiller bar is that it introduces flexibility in adjusting the delay to the cyclic controls since the rotor blades are now controlled by both fly bar tilting and a portion of cyclic controls.

Let $\bar{\beta}_{1c}$ and $\bar{\beta}_{1s}$ be the longitudinal and lateral first harmonic terms for the fly bar. The fly bar can be formulated using a first order dynamic system [8]:

$$\tau_s \dot{\bar{\beta}}_{1c} = -\bar{\beta}_{1c} - \tau_s q_B + \bar{d} \theta_{1s}^s \quad (2.87)$$

$$\tau_s \dot{\bar{\beta}}_{1s} = -\bar{\beta}_{1s} - \tau_s p_B + \bar{d} \theta_{1c}^s \quad (2.88)$$

where τ_s and \bar{d} are time constants of the fly bar and control derivative, respectively. While \bar{d} can be determined experimentally, the time constant τ_s is a function of the fly bar's lock number γ_s and rotor speed Ω :

$$\tau_s = \frac{16}{\gamma_s \Omega} \quad (2.89)$$

where lock number for the fly bar can be determined by the following equation:

$$\gamma_s = \frac{\rho a_{\text{bar}} c_{\text{bar}} (r_2^2 - r_1^2)}{I_b^{\text{bar}}} \quad (2.90)$$

where r_2 and r_1 are the outer and inner radii of the fly bar, respectively. θ_{1c}^s and θ_{1s}^s represent longitudinal and lateral cyclic controls at the rotating swashplate. The cyclic controls at the rotor blades are expressed as

$$\theta_{1c} = \theta_{1c}^s + k_{\text{bar}} \bar{\beta}_{1c} \quad (2.91)$$

$$\theta_{1s} = \theta_{1s}^s + k_{\text{bar}} \bar{\beta}_{1s} \quad (2.92)$$

where k_{bar} is the fly bar bearing determined by the geometry of the mechanic mixer. Experimentally, k_{bar} is not difficult to measure. Setting both θ_{1c} and θ_{1s} to zero followed by tilting the fly bar flapping angle, the value of k_{bar} is the ratio of measured changing pitch angle along the blade to the fly bar flapping angle.

2.4 Helicopter Performance Prediction

Endurance and range are two important performance indices in helicopter flight. Both indices can be directly derived from helicopter power calculation. Total power required for a helicopter comes from three difference sources:

- **Main Rotor Power:** This is the most dominant component in the total power consumption. This rotor power includes induced power, profile power, and parasite power. Induced power is associated with rotor thrust production, which is considered as *useful* power. Profile power is required to turn the rotor in viscous air. Parasite power is needed to overcome the helicopter drag including fuselage and empennage.

- *Tail Rotor Power:* As the tail rotor is used to counter the main rotor torque, its power consumption can be derived based on the torque and its own rotational speed. Typically, the tail rotor's power is approximately 10% of main rotor's power at hover and low speed flight. As the helicopter transits to high speed, the vertical fin may be effective enough to offset an essential portion of the main rotor torque. Thus, the required power by the tail rotor typically drops as the flight speed increases.
- *Ancillary Power:* This is to calculate the power used to drive ancillaries such as hydraulics and generators. The ancillary power also takes into account various power losses presented in the whole system. Typically, ancillary power counts for 5 – 10% of the total power required.

A formula for computing main rotor power is shown as follows:

$$P = \kappa T V_i + \rho A (\Omega R)^3 \frac{\sigma c_{d0}}{8} (1 + 4.6 \mu^2) + DV \quad (2.93)$$

The first component in the power equation is the induced power. An empirical factor κ is associated with this component to account for wake tip loss, nonuniform inflow and other losses. A number of values for the factor κ are suggested in the literature with a typical value taken to be 1.15. Rotor thrust T can be approximated as W at hover and low speed flight, or $\sqrt{W^2 + D^2}$ for moderate and high speed flight. A complete formula for the calculation of induced velocity V_i is provided in Sect. 2.3. However, this formula is not easy to solve especially in forward flight and a Newton–Raphson algorithm is required. Fortunately, this formula can be simplified with respect to the speed regime:

$$V_i = \begin{cases} \sqrt{\frac{W}{2\rho A}}, & \text{hover} \\ \frac{T}{2\rho AV}, & V > 0.1\Omega R \end{cases} \quad (2.94)$$

The second component in (2.93) is the profile power. A typical value of drag coefficient c_{d0} is taken as 0.0087. However, this value is obtained with ideal testing conditions and for a blade in near perfect form. In reality, a 50% increase of $c_{d0} = 0.0087$ is usually adopted for conservative purposes. The last component in (2.93) is the parasite power, which is mainly contributed from fuselage, empennage, and rotor hub. A detailed description of parasite drag in forward flight can be referred to in [84]. Values for equivalent flat-plate area S_{Ref} range from $10ft^2$ for small helicopters to $50ft^2$ for large utility helicopters. In the case of UAVs, the values can vary from $0.5ft^2$ to $2ft^2$ depending on the UAV size, exposure of mechanical linkages, and landing systems.

Power consumption due to the tail rotor can be calculated using (2.93) with minor modifications. The parasite power component is dropped off in the calculation, while parameters for main rotor are exchanged with those for tail rotor. A simple way of computing tail rotor power is to take 10% of the main rotor power for hover and 5% high speed.

Table 2.1 RMAX general data for power prediction

Rotor diameter	3115 mm
Number of blades	2
Blade chord	138 mm
Rotor speed	830 RPM
Gross weight	88 kg

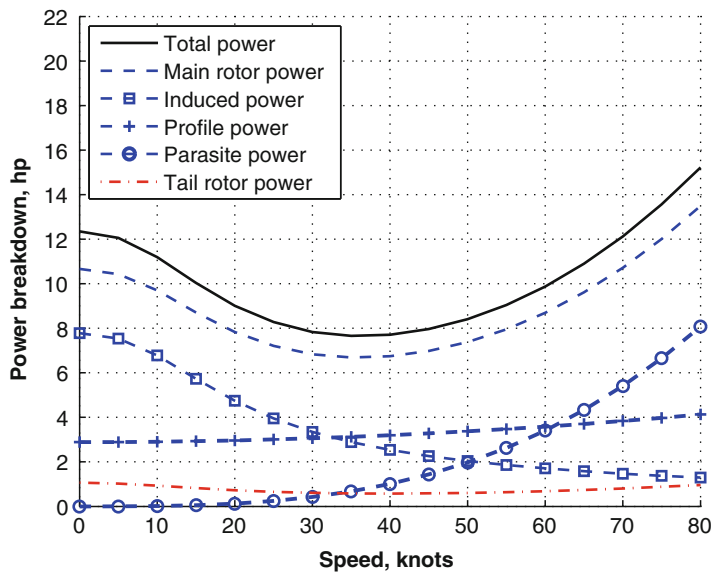


Fig. 2.7 Power prediction for a Yamaha RMAX helicopter

An example is now provided to illustrate power prediction for a hobby helicopter, i.e., the Yamaha RMAX helicopter. The RMAX is a popular radio-controlled rotary-wing platform. It has been widely used in universities and research institutes as a testbed for a range of activities including nonlinear modeling, flight control, and system identification [91]. General data for the RMAX helicopter is provided in Table 2.1. Other parameters required for power calculation include: $\kappa = 1.15$, $c_{d0} = 0.013$ (50% more than the nominal value of 0.0087 for NACA 23012 airfoil), $S_{\text{ref}} = 1.5\text{ft}^2$, and $\eta_{\text{auxillary}} = 0.9$.

The U-shaped total power curve in Fig. 2.7 illustrates power required for the RMAX in a straight and level flight at sea level. Induced power is the dominant component at hover, but reduces significantly as the speed increases. Profile power gradually increases over the speed to reflect the growing effects from compressibility at the advancing blade and stall and reverse flow at the retreating blade. Parasite power will be dominant at high speed flight as it is proportional to V^3 . The values for tail rotor power are almost flat when the effect from the vertical fin is not considered here. However, in the presence of a vertical fin, the tail rotor power in general decreases with the increase of flight speed.

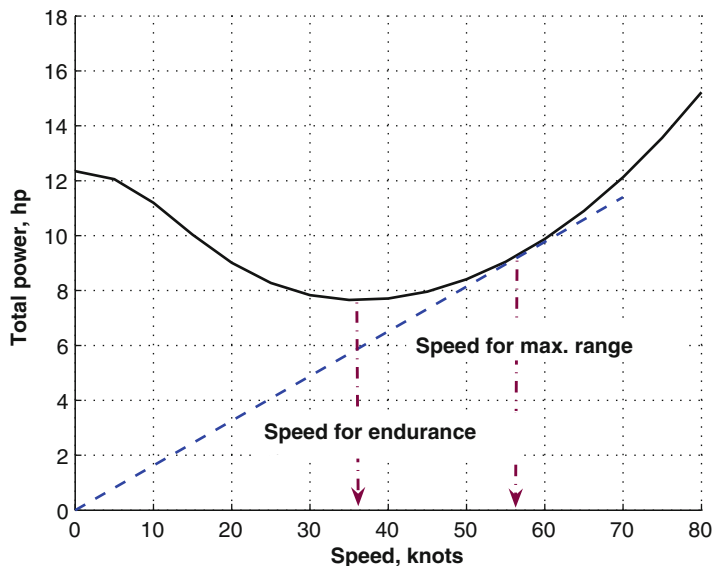


Fig. 2.8 Determination of endurance and range

Maximum endurance can be achieved when a helicopter operates at a flight speed with the least required power. As observed from Fig. 2.8, this speed can be found at the bottom of the U-shaped power curve (37 knots in Fig. 2.3). Interestingly enough, the endurance speed does not coincide with the minimum drag point, which can be graphically found by drawing the tangent to the U-shaped power curve. A helicopter can achieve the best range at this point as it corresponds to the minimum value of the ratio P/V , which can be further interpreted as the best lift-to-drag ratio. In general, endurance and range can not be achieved at one speed and the endurance speed is always slower than the range speed.

2.5 Conclusion

As stated in Sect. 2.1, we provided a modeling platform for a general class of rotor-wing vehicles. These rotary-wing vehicles include but are not limited to the compound helicopter, the coaxial helicopter, the helicopter with vectored thrust open propeller (VTOP), the helicopter with vectored thrust ducted propeller (VTDP), autogyro (also known as gyrocopter, autogiro, and gyrodyne), the tilt-rotor aircraft, and the tilt-wing aircraft.

The common feature of these vehicles that they have at least one main rotor. Some have more than one main rotor, like the coaxial helicopter, the tilt-rotor,

Table 2.2 Modular-based Modeling for rotor-wing vehicles

Unconventional rotor-wing vehicles	Distinctive features compared with classical helicopters
Compound helicopter	Two secondary rotors: one for a tail rotor and another for a pusher propeller; tail rotor used to counter main rotor torque at low speed; pusher propeller used to provide a forward thrust; wing module required to share lift with the main rotor; interference between main rotor and wing needed.
Co-axial helicopter	Two main rotors; interference between two main rotors crucial: interference velocity at lower rotor hub due to upper rotor superimposed to the induced velocity for lower rotor and vice versus; no horizontal and vertical tails required.
Vectored thrust open propeller	A propeller as the secondary rotor: tail rotor at low speed and a propeller at high speed; swivel angle of open propeller treated as a trim variable; wing required; one less secondary rotor compared to compound helicopter.
Vectored thrust ducted propeller	Similar to VTOP except the swivel angle for open propeller in VTOP changed to rotating angle for the vane in VTDP; aerodynamic effect from duct considered.
Tilt-rotor aircraft	Two main-rotor modules required; interference between the main rotor and the wing necessary when operating in the helicopter mode.
Tilt-wing aircraft	Two main-rotor modules required; FCS related to wing tilting required.
Autogyro	Main rotor operating in auto-rotation mode with induced velocity in the steep descent regime; main rotor rotational degree-of-freedom necessary; use secondary rotor module for propeller; interference from propwash to rudder essential for directional effectiveness at low speed.

and the tilt-wing. Some have more than two rotors, like the compound helicopter. Some instead have an extra propeller module, including the autogyro, the VTOP, and the VTDP. Besides the differences in the rotor system, interference can be critical in some cases. For example, whether there is interference between the rotor and the wing is a distinct feature that separates the tilt-rotor aircraft from the tilt-wing aircraft. For an autogyro, when its rudder is immersed in the propwash, it could have added directional capability. Distinctive features of those rotary-wing vehicles are listed in both Table 2.2.

The key concept in modeling the rotary-wing vehicles is to follow the diagram in Fig. 2.2. For one type of vehicle, its associated modules may be different from those of the classical single main-rotor configuration. However, they can be either special cases of those modules illustrated in Sect. 2.3 (for example, a propeller module),

or duplicated modules with minimum differences (for example, two identical rotors on a tilt-rotor aircraft with opposite rotational directions). Once established, those modules produce forces and moments to the general equations of motion. The general equations of motion will update its motion variables based on the forces and moments, and transmit those motion variables back to each individual module.

Modeling, Control and Coordination of Helicopter
Systems

Ren, B.; Sam Ge, S.; Chen, C.; Fua, C.-H.; Lee, T.H.

2012, XVI, 232 p., Hardcover

ISBN: 978-1-4614-1562-6